6

Applications of Optical Resonance to Biological Sensing and Imaging: II. Resonant Cavity Biosensors

M.S. Ünlü, E. Özkumur, D.A. Bergstein, A. Yalçin, M.F. Ruane, and B.B. Goldberg

6.1 Multianalyte Sensing

Interrogating binding interactions between proteins, segments of DNA or RNA, and biospecific small molecules is critically important for a great number of applications in biological research and medicine. Microarray technology has emerged over the past decade to address applications that seek to measure thousands or even millions of binding interactions at once. A microarray consists of a solid support, or substrate, with multiplicity of spots on its top surface each containing a different type of fixed capturing molecule. A sample solution containing unknown target molecules, or analytes, is introduced to the microarray surface typically via a small fluid chamber or flow cell. The amount of target material bound to any feature after washing the array gives an indication of the affinity between the target and capturing agent at that spot. There are a number of important applications in biological research that benefit from microarray throughput such as gene expression profiling or antigen–antibody interaction monitoring. Aside from research applications, microarrays may play a crucial role in a new era of medical diagnostics. Biomedical research is continuing to point toward molecular biomarkers that can be used to help doctors diagnose diseases sooner, with greater accuracy, and provide information that helps doctors personalize treatment plans.

Present microarray technology requires that the target molecules in the sample solution be labeled or attached with a fluorescent dye molecule for the purpose of determining how much target material has bound to each microarray feature using a fluorescence detector. The need to label the target molecules to visualize the results is a significant shortcoming of present technology and has been described previously [1–4]. In general, fluorescent labeling may suffer from bleaching of the labels, quenching effects from the surface, or low contrast between the label and the autofluorescence of the microarray substrate. In addition, proteins in particular may suffer from altered binding properties once they are labeled. For these reasons, label-free detection for

both DNA and protein is preferred, particularly for use in medical diagnostics where variation and cost must be minimized.

A vast number of label-free detection techniques have surfaced over the last decade or two to address the problems of label-based detection [5–16]. The important figures of merit for these techniques are sensitivity to bound targets, throughput (number of features evaluated in a single test) and the ability to scale throughput, and cost per test. Sensitivity is often quantified by mass per area ($\mathrm{pg\,mm^{-2}}$) or average height (pm) where 1 pm corresponds to roughly $1\,\mathrm{pg\,mm^{-2}}$ for protein or DNA [17–25].

6.2 Resonant Cavity Imaging Biosensor

6.2.1 Detection Principle

Two partially reflecting substrates are positioned such that their reflecting surfaces face each other and form the optical cavity (Fig. 6.1) [26]. The tunable wavelength laser light is collimated and incident from the back of one of the reflectors. The wavelength of the laser is swept in time and at specific wavelengths the resonant condition of the cavity is met, the light resonates inside the cavity and couples out. Beyond the cavity, the transmitted light is imaged on a camera, so that the resonant response at each location of the cavity is recorded by a corresponding pixel on the camera. The probe biomolecules are patterned on one of the reflector surfaces. When target biomolecules bind to their specific capturing agents, the local resonant response shifts in

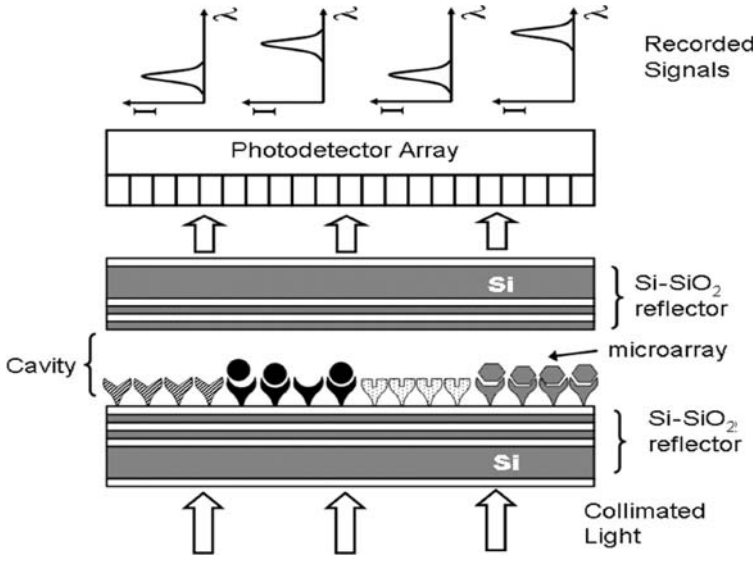

Fig. 6.1. Resonant cavity imaging biosensor (RCIB) setup.

wavelength. The presence of biomolecules bound to the surface is fundamentally detected by a small perturbation of the electric field inside the cavity. The effect of a slight phase delay is amplified by the resonant behavior of light within the cavity. The cavity enhancement can provide a significant sensitivity improvement over interference techniques that do not benefit from a high finesse optical cavity. The reflectors can be constructed with alternating dielectric layers of silicon and SiO_2 and may end with a layer of SiO_2 that allows the surface immobilization chemistries that are developed for glass slides to be used. The use of a parallel optical cavity, tunable wavelength laser, and a digital camera allows high throughput. Aside from the alignment and stability of the reflectors, and the internal operation of the tunable laser, there are no moving parts in the setup. Additionally, the reflectors described here may be made very inexpensive and hence disposable. In the present implementation, the cavity is formed with reflectors fabricated from alternating layers of Si and SiO_2, constituting a Bragg grating (Fig. 6.2) [27], and the wavelength of light is varied between 1,510 and 1,515 nm. The electric field distribution in the cavity forms a standing wave pattern with a minimum at the Si surface of the reflectors. It is beneficial to place the sensing surface on an approximately quarter wavelength thick layer of similar low-index material, namely SiO_2. Adding this extra oxide layer brings the binding surface some distance into the cavity where the field is maximum (Fig. 6.3). When it is placed at the field maximum, the sensing layer interacts with the highest number of photons and slight thickness changes will have a maximum effect on the field distribution, thereby shifting the resonant wavelength a maximum amount. If the sensing surface is positioned at a field minimum, small changes on the surface will have no effect on the resonant cavity and will therefore be undetectable. Adding an extra layer of SiO_2 also has the previously mentioned benefit of providing

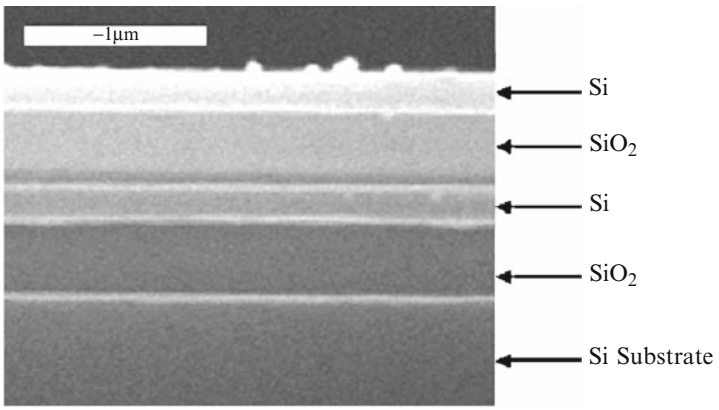

Fig. 6.2. The Bragg structures that are used as the reflectors in RCIB setup with alternating layers of 1/4 wavelength thick Si and 3/4 wavelength thick SiO_2. The image is taken with SEM.

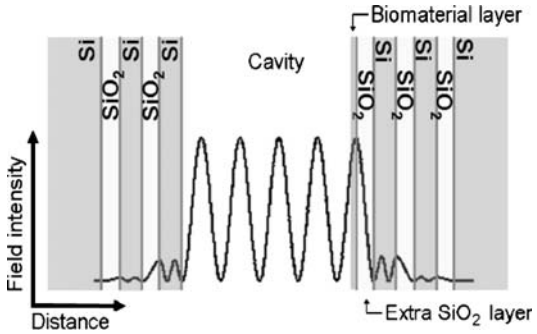

Fig. 6.3. Electric field pattern in the optical cavity.

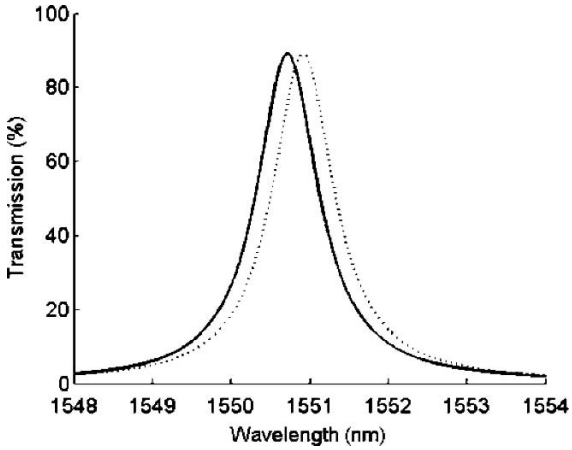

Fig. 6.4. Simulation of the transmittance of the cavity. The reflectors are 40.0 μm apart from each other with air in between. A final SiO_2 layer is included and shift corresponds to 5 nm step on the oxide.

a chemically compatible surface for microarray fabrication. Simulation of the cavity transmittance vs. wavelength with changing top surface oxide thickness is plotted in Fig. 6.4. Simulation was done in Matlab using the matrix method for calculating transmittance through layered media [28].

6.2.2 Experimental Setup, Data Acquisition, and Processing

An RCIB setup has been constructed. The illumination source is an IR tunable laser with a fiber-coupled output. Light is coupled into the system with a SMF-28 fiber and collimated to 10 mm FWHM. All the optics are antireflection coated to avoid interference effects. The laser power is set to 15 μW, and the wavelength is continuously swept from 1,510 to 1,515 nm in 10 s during data collection. The reflectors, which are 15 mm by 15 mm, are placed 40 μm apart

from each other. One reflector is mounted on a tip-tilt stage to bring the reflectors parallel. The second reflector is mounted on a translational stage to adjust the reflector separation. The transmission from the cavity is imaged on an indium–gallium–arsenide (InGaAs) sensor array with 5 × magnification and an aperture setting the NA to 0.1. With these settings, $12 \times 12\,\mu m^2$ areas are imaged on the $60 \times 60\,\mu m^2$ pixels of the sensor array, which has 128 × 128 pixels. The laser wavelength is swept at a rate of $0.5\,nm\,s^{-1}$ while the camera captures images at a rate of 30 fps. Images are digitized to 12 bits (4,096 gray-levels) and transferred to a PC.

These data are transferred to Matlab and fit using several different methods. There is a trade-off between the accuracy and the speed with which the data can be fit. A more accurate (noise-resilient) curve fitting method is to fit the data to resonant line shape given by (6.1), which models a simple resonant cavity where

$$T = \frac{n_i}{n_f}\left|\frac{t^2 e^{jkd}}{1 - r^2 e^{-2jkd}}\right|^2, \tag{6.1}$$

n_i and n_f are the refractive indices in and beyond the cavity, t and r are the transmission and reflection coefficients, respectively, of the reflectors, k is the wavenumber inside the cavity, and d is the reflector separation (Fig. 6.5). Further image processing subtracts the curvature inherent to the reflectors. Finally, a surface profile of small height variations on the SiO_2 surface can be obtained.

6.2.3 Experimental Results

The system sensitivity was tested by imaging etched features on the oxide surface (Fig. 6.6). The reflector that has a SiO_2 layer on top is used as the

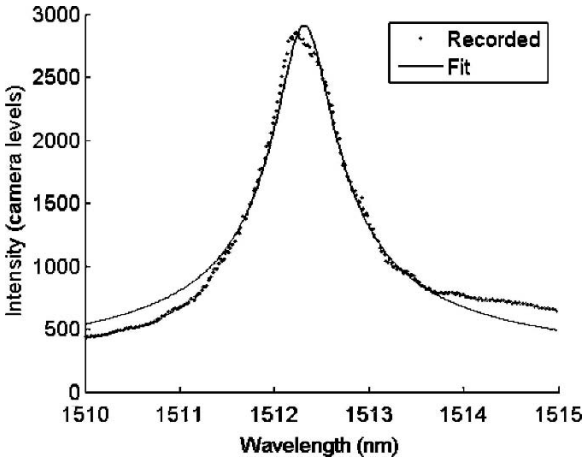

Fig. 6.5. Resonant curve recorded and fitting to this data using (6.1).

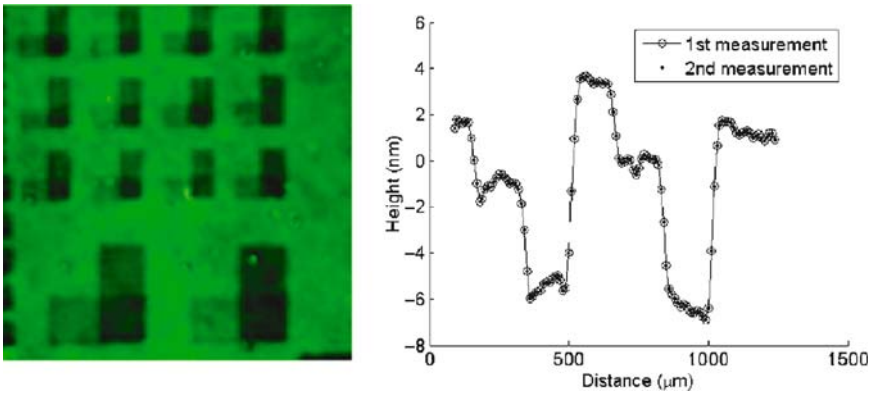

Fig. 6.6. *Left*: RCIB scan of the overlapping boxes. *Right*: Line cut of the image in two consecutive measurements.

sensing surface. Standard photolithography and wet (BOE) etching were used to pattern these features on the surface. Two overlapping rectangles, with depths of 3 and 6 nm were etched resulting in four regions with different oxide thickness; not etched, 3 nm deep, 6 nm deep, and 9 nm deep etched. These values are consistent with the AFM measurements of the same sample. System repeatability was tested by making consecutive measurements of the same sample. Averaging boxes measuring 5 pixels by 5 pixels, or an area of $50 \times 50\,\mu m^2$, the RMS deviation in consecutive measurements was 0.01 nm (Fig. 6.6).

6.2.4 Spectral Reflectivity Imaging Biosensor

The phase delay added by extra material can also be imaged using a simpler approach. We propose a surface profilometry technique to be used as a label-free microarray imaging device. Spectral reflectivity imaging biosensor (SRIB) uses wavelength dependent reflectivity of a silicon substrate with thick thermally grown SiO_2(5–10 μm), to accurately find the film thickness at tens of thousands of different spots, and thus image the surface profile. This technique, having a much lower finesse, is expected to be less sensitive than RCIB, but should be more robust and offer higher throughput. A collimated laser beam that can be tuned from 764 to 784 nm is reflected from a pellicle beam splitter and is incident on the sample surface (Fig. 6.7). At any fixed wavelength, reflection from the sample is imaged on a CCD camera (camera pixel size is 13.7 μm and the magnification of the imaging system is 2.3). Then the wavelength is stepped, and another image is taken. Repeating this through the sweeping range of the laser, one can form a spectral reflectivity curve for every $36\,\mu m^2$ area on the sample in the field of view. The separate

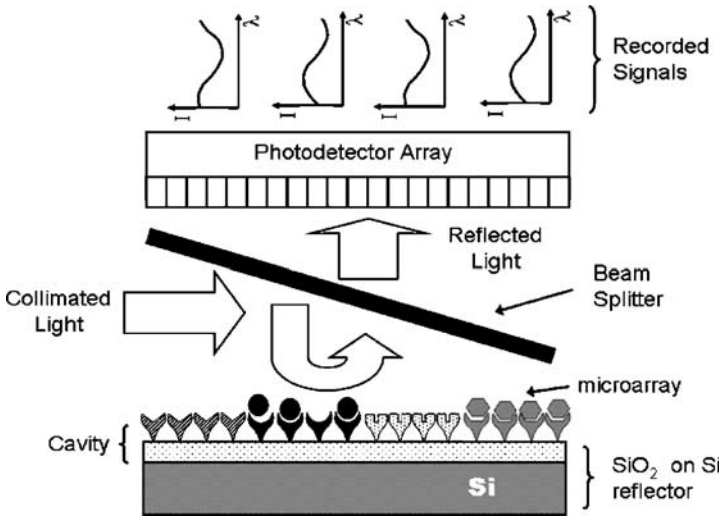

Fig. 6.7. Spectral reflectance imaging biosensor diagram.

reflections from oxide and silicon surfaces form an interference pattern and an exact oxide thickness corresponding to each pixel is found by curve fitting the recorded data.

Reflection of a single layer can be well estimated by Airy's formulas [28]. The reflection coefficient for an incoming field is given by:

$$r = \frac{r_{12} + r_{23}e^{-2i\phi}}{1 + r_{12}r_{23}e^{-2i\phi}} \tag{6.2}$$

$$\phi = \frac{2\pi d}{\lambda} n_{\mathrm{SiO_2}} \cos\theta, \tag{6.3}$$

where r_{12} and r_{23} are the Fresnel reflection coefficients from the SiO_2 surface and SiO_2-Si interface, respectively, and ϕ is the optical phase difference between the two reflections. Here, d is the SiO_2 thickness, n_{SiO_2} is the refractive index of SiO_2, λ is the wavelength of the incident light, and θ is the incidence angle to the SiO_2–Si interface, which will be 0° for perpendicular incidence. Curve fitting tools are used to fit this equation to the recorded data at each pixel and to find the d. The setup was tested with etch marks of overlapping rectangles that was mentioned in the previous section. Silicon wafers with 6.1 μm of thermally grown SiO_2 were etched by photolithographic techniques. Three different depths of etch steps were created on the sample, which were 4, 12, and 16 nm, and their depths were confirmed with AFM scans. The sample was then imaged by SRIB, and data were processed with curve fitting. A line-cut from the image can be seen in Fig. 6.8. These etch marks were imaged with an accuracy of 0.5 nm.

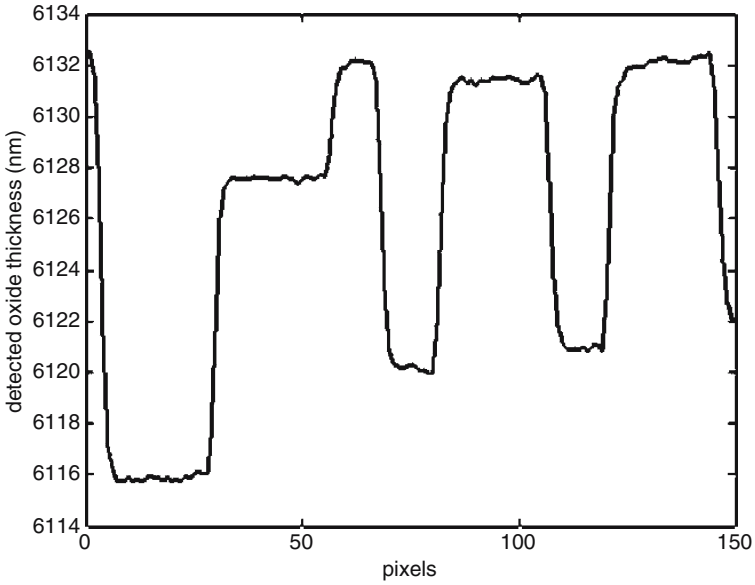

Fig. 6.8. Line-cut from a processed image taken by the SRIB setup. Etch marks at three different heights are seen: 4, 12, and 16 nm. The thickness of the oxide was ∼6,130 nm, initially.

Although the present data show that the system can image 250 spots with subnanometer sensitivity, balancing the laser intensity fluctuations and using a better imaging system is expected to improve sensitivity to 0.1 nm with more than 10,000 spots.

6.3 Optical Sensing of Biomolecules Using Microring Resonators

6.3.1 Basics on Microring Resonators

Integrated devices featuring resonant microcavities with high quality factors (Q) such as toroids, disks, rings, and spheres have been used as add-drop filters, optical switches, and in laser applications [29–33]. These devices have recently become popular for research in biochemical sensing [34–38] as the demand for highly sensitive and compact devices to detect biomolecules increased. Light is confined within the microring cavities by total internal reflections resulting in high Q resonant modes. When the refractive index of the cladding or the outside medium changes (e.g., due to binding of molecules), a new guiding condition is obtained for the mode, causing a shift in the resonant wavelength.

Microring resonators provide sensitivities comparable to surface plasmon resonance because of their high Q (∼12,000 in this study) [16,39], and they are robust and can be mass-manufactured using well-established silicon-integrated circuit fabrication techniques. However, they lack the very high-throughput potential that is demonstrated with RCIB.

The sensitivity of the system presented here is quantified through measurement of resonance shifts induced by a change in the refractive index of the medium (a bulk change). Additionally, sensing of biomolecules is demonstrated through observation of the change in resonant condition caused by molecular binding of the well-documented avidin–biotin couple on the surface.

6.3.2 Setup and Data Acquisition

The microring resonators used in this experiment are 60 μm in radius, and vertically coupled to waveguides (Fig. 6.9). The effective index of the cavity is measured as $n_{\text{eff}} \approx 1.5$ in deionized water (DI-H_2O) ambience, and the penetration depth for the guided mode at 1,550 nm in this environment is calculated as ∼360 nm. A fiber-coupled tunable wavelength IR laser is used as the light source. The cavity can support both TE and TM modes and with the use of a polarizer one of the modes is selected. An optical splitter placed after the polarizer separates the signal into two paths: one arm is chopped in free space at a frequency of 220 Hz and then coupled to the input waveguide of the microring resonator. The output waveguide is coupled to a photodetector as signal input. The second arm acts as the reference input to the photodetector for balanced detection. Common-mode noise cancellation

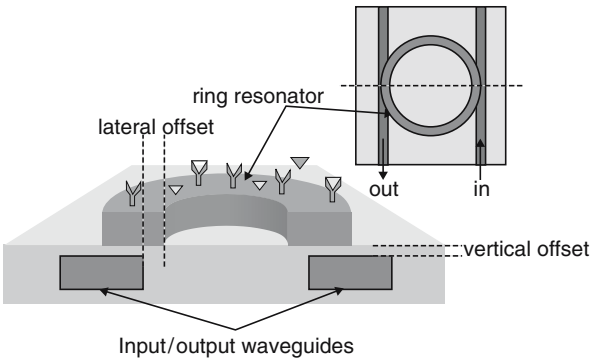

Fig. 6.9. Microring resonator is vertically coupled to input/output waveguides. Lateral and vertical offsets of the resonator allow control over the coupling coefficient. Receptor molecules are immobilized on the resonator surface, and target molecules are released on the surface in a solution during flow. The *top view* of the resonator is shown in the inset.

(mainly laser intensity fluctuations) is achieved through balanced detection, improving the signal-to-noise ratio, thus the overall system sensitivity. A flow-cell is used for controlled solution flow over the microring surface, and real time signal during solution flow is acquired and analyzed with LabVIEW. Direct measurement of a shift in resonance through repeated spectral scans is time consuming. Alternatively, the resonance shift can be measured indirectly by collecting data at a single wavelength and observing the intensity in real time, and the change in intensity can then be mapped to a shift in resonance. To obtain the maximum change in intensity due to a change in effective index, the wavelength at which the measurements are performed is selected to correspond to the point of maximum slope of the resonance curve. The high intensity stability necessary for these measurements is achieved by eliminating the noise components of laser output through balanced detection.

6.3.3 Data Analysis and Discussion

The bulk experiments to determine the sensitivity of the system were conducted by flow of a solution of known refractive index with respect to the refractive index of DI-H_2O that is used as a calibration reference. In Fig. 6.10, the measured shift in resonance with respect to a change in the refractive index of the medium (corresponding to various concentrations of phosphate buffered saline (PBS) solution) is plotted. Notice that the relation is highly linear. Using standard deviation δ (pm) of signal levels during PBS flow and the slope (m) of the plot in Fig. 6.10, the limit of detection (LOD) for a change in refractive index can be approximated as $\mathrm{LOD}(n)=3\delta\,\mathrm{m}^{-1}$. We conclude that $\mathrm{LOD}(n) = 1.8 \times 10^{-5}$ refractive index units (RIU) for our setup. The experiment to demonstrate detection of biomolecules consists of two parts: binding of biotinylated lectins to an avidin covered surface, and breaking the avidin–biotin bonds for surface regeneration. For binding, 3.5 μM biotinylated lectin solution is flowed over the surface. Once the signal level reached by the binding of biotin molecules to avidin covered surface is stabilized, DI-H_2O is flowed to wash away the unbound molecules. For surface regeneration, the surface is first washed with a chemical pH-7 buffer that breaks the avidin–biotin bonds, and then with DI-H_2O. The real-time intensity recording of binding/regeneration processes is shown in Fig. 6.11. The actual amount of change in the signal is measured between levels of DI-H_2O flow before and after the introduction of biotinylated lectin solution. At these levels, the outside medium is identical, so the change in intensity is caused only due to binding of molecules. The signal level at the end of the regeneration phase is close to the initial level indicating that partial recovery of surface is achieved.

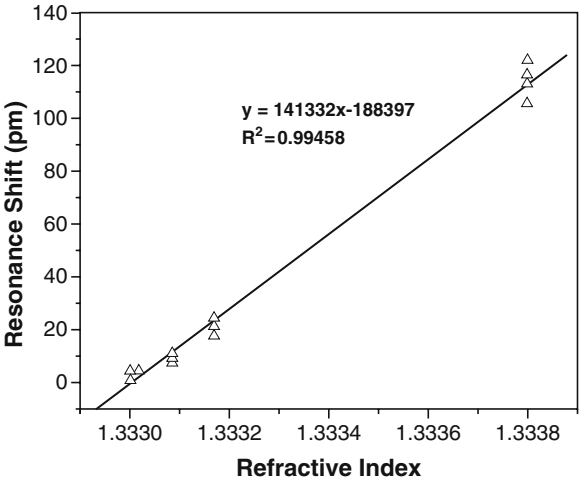

Fig. 6.10. Shift of resonance is linearly related to change in refractive index. The slope of the plotted curve is used to determine the limit of detection for refractive index changes.

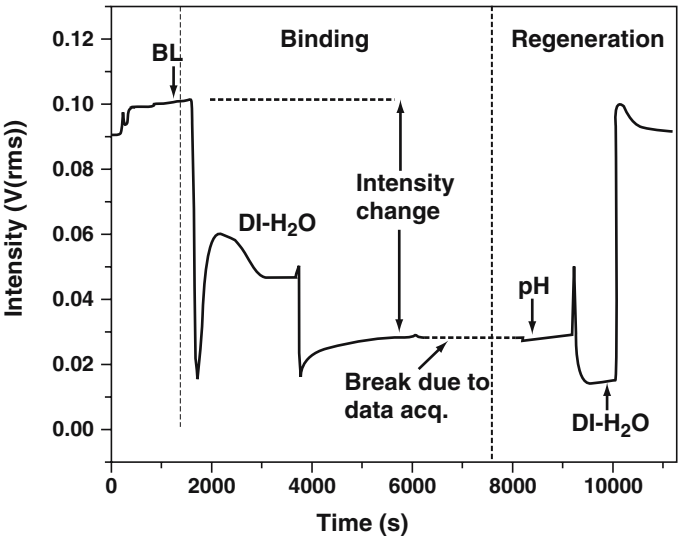

Fig. 6.11. The detected intensity in a real time binding experiment is plotted. The plot illustrates both binding and regeneration phases (BL: biotinylated lectin solution, DI-H_2O: deionized water, pH: pH-7 buffer). Binding efficacy is only measured between the signal levels when DI-H_2O is flowed across the sensor.

6.4 Conclusions

We have presented three optical techniques aimed at molecular sensing that employ optical resonance. A planar optical resonant cavity is used in the case of RCIB, where the high finesse of the optical cavity can provide high sensitivity, while the planar configuration tied with a camera and tunable laser can provide for simultaneous detection from many parallel locations. The technique was demonstrated using nanometer scale etches in a SiO_2 surface that model microarray features. We have also presented a second technique that observes the wavelength-dependent reflectivity from a silicon substrate with a thermally grown oxide layer to detect molecules binding to the top oxide surface. In this case, the Fresnel reflection measured can be considered to be the result of a low finesse optical cavity formed by the oxide layer together with the bound molecules. The benefit of this technique compared with the high finesse RCIB technique is that the monolithic structure avoids the difficulty maintaining the reflector alignment necessary in the latter technique. In the final technique presented, microring resonators employ a very strong resonant coupling to achieve very high sensitivity at the cost of added complexity and a larger minimum feature size.

Acknowledgments

The authors acknowledge Boston University Office of Technology Development for their support, the National Institute of General and Medical Sciences (NIH R21 GM 074872-02), and the Army Research Laboratory (ARL) for their support under the ARL Cooperative Agreement Number DAAD17-99-2-0070 and under the AMCAC-RTP Cooperative Agreement DAAD19-00-2-0004. The authors also thank Dr. Brent Little and the Little Optics Division of Nomadics Inc. for providing the microring resonator devices. The views and conclusions contained in this document are those of the authors and should not be interpreted as representing the Laboratory or the US Government.

References

1. S. Niu, R.F. Saraf, Smart Mater. Struct. **11**, 778 (2002)
2. R. Nadon, J. Shoemaker, Trends Genet.**18**, 265 (2002)
3. M.A. Cooper, Nat. Rev. Drug Discovery **1**, 515 (2002)
4. M. Schena, *Microarray Biochip Technology,* (Eaton Publishing, Natick, 2000)
5. J.M. Brockman, B.P. Nelson, R.M. Corn, Annu. Rev. Phys. Chem. **51**, 41 (2000)
6. K. Usui-Aoki, K. Shimada, M. Nagano, M. Kawai, H. Koga, Proteomics **5**, 2396 (2004)
7. C. Worth, B.B. Goldberg, M.F. Ruane, M.S. Ünlü, IEEE J. Select. Top. Quantum Electron. **7**, 874 (2001)
8. W. Lukosz, Biosensors Bioelectron. **6**, 215 (1991)
9. H. Nygren, T. Sandström, M. Stenberg, J. Immunol. Meth. **59**, 145 (1983)

10. T. Sandström, M. Stenberg, H. Nygren, Appl. Opt. **24**, 472 (1985)
11. J. Piehler, A. Brecht, G. Gauglitz, Anal. Chem. **68**, 139 (1996)
12. P.I. Nikitin, M.V. Valeiko, B.G. Gorshkov, Sensors Actuators B **90**, 46 (2003)
13. J.P. Landry, X.D. Zhu, J.P. Gregg, Opt. Lett. **29**, 581 (2004)
14. J. Lu, C.M. Strohsahl, B.L. Miller, L.J. Rotherberg, Anal. Chem. **76**, 4416 (2004)
15. S. Chan, Y. Li, L.J. Rothberg, B.L. Miller, P.M. Fauchet, Mater. Sci. Eng. C **15**, 277 (2001)
16. A. Yalcin, K.C. Popat, J.C. Aldridge, T.A. Desai, J. Hryniewicz, N. Chbouki, B.E. Little, O. King, V. Van, S. Chu, D. Gill, M.F. Anthes-Washburn, M.S. Ünlü, B.B. Goldberg, IEEE J. Select. Top. Quantum Electron. **12**, 148 (2006)
17. L. Moiseev, M.S. Ünlü, A.K. Swan, B.B. Goldberg, C.R. Cantor, Proc. Natl. Acad. Sci. **103**, 2623 (2006)
18. L.K. Wolf, Y. Gao, R.M. Georgiadis, Langmuir **20**, 3357 (2004)
19. L. Moiseev, C.R. Cantor, A.K. Swan, B.B. Goldberg, M.S. Ünlü, Proc. Int. Soc. Opt. Eng. Nanobiophotonics Biomed. Appl. **5331**, (2004)
20. J.J. Ramsden, Opt. Biosens. J. Mol. Recogn. **10**, 109 (1997)
21. J.A. DeFeijter, J. Benjamins, F.A. Veer, Biopolymers **17**, 1759 (1978)
22. S.N. Timasheff, in *Handbook of Biochemistry and Molecular Biology,* vol. 3, ed. by G. Fasman (CRC Press, Cleveland, 1977), p. 372
23. P. Schaaf, P. Dejardin, A. Schmitt, Langmuir **3**, 1131 (1987)
24. T.M. Davis, W.D. Wilson, Anal. Biochem. **284**, 348 (2000)
25. S. Nui, A. Label-free, Ph.D. dissertation, Virginia Polytechnic Institute and State University, 2004
26. D. Bergstein, M.F. Ruane, M.S. Ünlü, in *International Semiconductor Device Research Symposium, Maryland, USA*, 7–9 December 2005
27. M.K. Emsley, O.I. Dosunmu, M.S. Ünlü, IEEE J. Select. Top. Quantum Electron. **8**, 948 (2002)
28. P. Yeh, *Optical Waves in Layered Media* (Wiley, New York, 1988)
29. B.E. Little, S.T. Chu, W. Pan, D. Ripin, T. Kaneko, Y. Kokubun, E.P. Ippen, IEEE Photon. Technol. Lett. **11**, 215 (1999)
30. M. Cai, G. Hunziker, K. Vahala, IEEE Photon. Technol. Lett. **11**, 686 (1999)
31. V. Van, T.A. Ibrahim, K. Ritter, P.P. Absil, F.G. Johnson, R. Grover, J. Goldhar, P.T. Ho, IEEE Photon. Technol. Lett. **14**, 74 (2002)
32. L. Yang, D.K. Armani, K.J. Vahala, Appl. Phys. Lett. **83**, 825 (2003)
33. B. Liu, A. Shakouri, J.E. Bowers, Appl. Phys. Lett. **79**, 3561 (2001)
34. K.J. Vahala, Nature **424**, 839 (2003)
35. R.W. Boyd, J.E. Heebner, Appl. Opt. **40**, 5742 (2001)
36. S. Arnold, M. Khoshsima, I. Teraoka, S. Holler, F. Vollmer, Opt. Lett. **28**, 272 (2003)
37. F. Vollmer, D. Braun, A. Libchaber, M. Khoshsima, I. Teraoka, S. Arnold, Appl. Phys. Lett. **80**, 4057 (2002)
38. J. Hryniewicz, N. Chbouki, B.E. Little, O. King, V. Van, S. Chu, D. Gill, in *Biophotonics/Optical Interconnects and VLSI Photonics/WBM Microcavities*, 2004 Digest of the LEOS Summer Topical Meetings, 33 (2004)
39. Bardin, I. Kasik, A. Trouillet, V. Matejec, H. Gagnaire, M. Chomat, Appl. Opt. **41**, 2514 (2002)